CHEMISTRY OF MATERIALS

ARTICLE

pubs.acs.org/cm

Ordered Mesoporous Carbon Composite Films Containing Cobalt Oxide and Vanadia for Electrochemical Applications

Mingzhi Dai,[†] Lingyan Song,[†,§] Jeffrey T. LaBelle,[‡] and Bryan D. Vogt*[,†]

[†]Chemical Engineering Program and [‡]School of Biological Health Systems Engineering, Arizona State University, Tempe, Arizona 85287, United States

Supporting Information

ABSTRACT: Mesoporous carbon composite thin films (<500 nm) containing cobalt and vanadium oxide were synthesized by triconstituent self-assembly using Pluronic F127 as template, phenol-formaldehyde oligomer (resol) as carbonizable precursor, and cobalt (or vanadyl) acetylacetonate (acac) for the metal source. The ordered mesostructure of the composite films was confirmed by both X-ray diffraction (XRD) and transmission electron microscopy (TEM). During pyrolysis at 800 °C to carbonize the film, the *d*-spacing decreases significantly because of uniaxial contraction; however addition of Co/V content leads to a decrease in the contraction from approximately 68% to 50%, which indicates the Co/V mechanically strengthens the framework. The decrease in contraction also leads to an increase in the average pore size by as much as 60%. Nanoparticles are found to be dispersed within the continuous carbon framework from both high resolution (HR)-TEM and scanning transmission electron microscopy (STEM); small sub-2 nm particles are observed in all cases for V containing films, while particles greater than 10 nm are found at high Co contents. In addition to these structural changes, the electrical conductivity of the mesoporous carbon film can be increased from 22 S/cm to approximately 40 S/cm by adding 10 wt % of either $Co(acac)_3$ or $VO(acac)_2$ in the precursor solution. The conductivity decreases as the organometallic content is further increased, but still remains quite conductive (19.6 S/cm for 50% $VO(acac)_2$). The addition of the transition metals also greatly enhances the electrochemical performance because of their pseudocapacitance. Even after 500 cycles, the composite films maintain a specific capacitance as high as 113 $F \cdot g^{-1}$ (for Co) and 159 $F \cdot g^{-1}$ (for V) in comparison to the neat carbon, which is initially approximately 22 $F \cdot g^{-1}$. These materials exhibit favorable electrochemical properties for potential energy storage applications such as insertion batteries and supercapacitors.

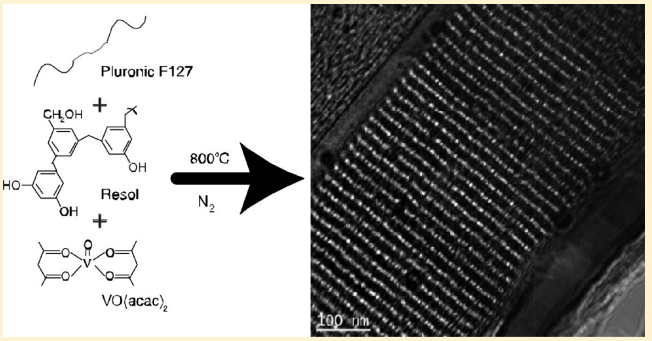

KEYWORDS: ordered mesoporous film, conductivity, block copolymer, supercapacitor, self-assembly

INTRODUCTION

Ordered mesoporous carbon materials have garnered significant attention because of their attractive properties such as electrical conductivity, chemical inertness, high surface area, uniform pore size, and biocompatibility.[1,2] These properties have led to proposed use of mesoporous carbons as catalyst supports,[3] sensors,[4] electrodes,[5] adsorbents for water remediation,[6] and active materials for energy storage[7] as examples. Ordered mesoporous carbon powders have been historically synthesized by nanocasting where a sacrificial (typically, silica) hard porous template is filled with the carbonizable precursor and then the template is dissolved after carbonization to yield an inverse replica.[8] More recently, soft templating approaches have been introduced that provide a more direct route to mesoporous carbons through organic−organic self-assembly.[9,10] These soft templating approaches can also be applied to fabricating mesoporous carbon films.[11,12]

There have been multiple routes developed to modify carbon to increase its functionality and/or performance especially for electrochemical applications.[3,13−18] For example, triconstitute self-assembly to form an ordered mesoporous carbon-silica nanocomposite where the silica is subsequently removed yields significant improvements in the electrochemical performance by increasing the Brunauer−Emmett−Teller (BET) surface area (from 650 to 2390 m^2/g) in comparison to an analogous soft templated carbon.[19] Alternatively, the carbon can be doped with nitrogen, phosphorus, or boron to significantly increase the electrochemical capacitance.[15,20] Similarly, incorporating metal oxide nanoparticles into the carbonizable precursor provides an alternative route to improved electrochemical performance.[3,14,29] However, the long-term electrochemical performance of these mesoporous carbon based materials for reversible Li storage appears to be limited in comparison to alternatives such as hollow, carbon coated SnO_2 nanoparticles.[22] The increased Li

Received: January 25, 2011
Revised: April 18, 2011
Published: May 10, 2011

capacity of some transition metal oxides, such as TiO_2, MnO_2, SnO_2, and V_2O_5, in comparison to carbon makes these metal oxides highly attractive for Li insertion battery electrodes.[23−27] However, their low electrical conductivity limits charge transfer and hence performance. Furthermore, the charge−discharge reversibility of bulk metal oxides is generally low because of the large volume changes that lead to pulverization of the active material upon successive cycling.[28] Addition of porosity in the material to enable expansion does provide some improvement in the cycling stability for Li battery applications,[29] but additional improvements in cyclability occur when the metal oxide is coated with a thin carbon layer because carbon can function as a physical buffering layer for large volume change through the so-called cushion effect.[28] These results would suggest that mesoporous carbon composites could provide a route to high performance anodes for Li battery technology.

However, there are few reports of such mesoporous nanocomposite materials.[21,30,31] For example, Patel et al. illustrated that the electrochemical pseudocapacitance of disordered mesoporous carbon can be dramatically improved by the addition of MnO_2 nanoparticles.[21] Ordered mesoporous nanocomposites with well-defined geometry and pore size could provide improvements in the ion transport and surface area, which in turn would lead to improved performance. Ordered mesoporous carbon−sulfur materials prepared by infiltration of sulfur into the micropores have exhibited high performance for Li/S battery applications.[13] Recently, Aksay and co-workers reported surfactant assembled graphene-tin oxide nanostructures that exhibit near theoretical specific energy density for Li insertion, as the electrochemical properties of the nanocomposites can be improved by increasing the conductivity of the electrode materials with graphene and by stabilizing the electrode structure with a good electric contact between SnO_2 and conductive graphene during the charge−discharge process.[32] However, this synthesis can be quite challenging because of multiple length scales of the building materials, while triconstituent self-assembly to synthesize mesoporous nanocomposites is quite facile.[18] This self-assembly approach can also be applied to the assembly of carbonizable oligomers, metal alkoxides (sol−gel), and surfactants/block copolymers templates to yield ordered mesoporous materials with discrete metal oxide and carbon domains within the pore wall.[18,30] For the carbon-titania nanocomposites formed by triconstituent self-assembly, modest reversible capacities are reported,[30] but to achieve a high capacity for Li battery applications alternative metal oxides are required. One potential difficulty in extending this triconstituent assembly approach is controlling the interactions between the carbonizable oligomer, metal oxide sol, and templating agent. For some transition metal oxides such as tin oxide, it is difficult to even obtain an ordered structure for the pure material without complex processing.[33] Alternatively, metal salts have been utilized to form nanoparticles within carbon aerogels,[34] but these salts could interfere with self-assembly of the surfactant, which may lead to disordered carbon framework or decrease the porosity. Recently, Zhao and co-workers have demonstrated that ordered mesoporous carbon-MgO composites can be synthesized using magnesium nitrate, but the MgO nanoparticles can be larger than the pore walls and extend into the pores especially at high loadings.[35]

Alternatively, thermolysis of organometallic compounds is an effective route to synthesis of carbon coated metal nanoparticles,[27] but these are typically isolated large nanoparticles. The carbon shell and morphology of the nanoparticles are dependent upon the ligands and their carbonization. By proper selection of organic ligands on cobalt, thermolysis and controlled oxidation leads to carbon coated cobalt particles with excellent Li storage properties.[27] One such ligand is acetylacetonate (acac), which has also been utilized in controlling condensation rates for mixed metal oxides formed by sol gel chemistry.[36,37] This stability of metal (acac) should provide a wide processing window for incorporating transition metals into ordered mesoporous carbons.

In this work, the triconstituent synthesis method for fabrication of ordered mesoporous carbon composites is extended to include cobalt and vanadium oxides by using $Co(acac)_3$ and $VO(acac)_2$ as precursors. Evaporation induced self-assembly (EISA) of low-molecular weight phenolic resin (resols),[38,39] commercially available triblock copolymers (Pluronic F127) and metal (acac) is utilized to form highly ordered mesoporous carbon composite thin films after pyrolysis at 800 °C. The porous morphology of the films is investigated by X-ray diffraction, transmission electron microscopy (TEM), and ellipsometric porosimetry. Additionally, the electrical and electrochemical properties of these films are examined as a function of composite film composition. These results illustrate the versatility of the triconstituent assembly approach for fabrication of ordered mesoporous carbon composites with potential applications in catalysis, energy storage, and sensing.

EXPERIMENTAL SECTION

Materials. A triblock copolymer surfactant, Pluronic F127 (M_w = 12 600 g/mol, PEO_{106}-PPO_{70}-PEO_{106}, BASF), was used to template the carbon-based composite mesostructures. Sodium hydroxide (NaOH, Aldrich), phenol (Aldrich), and formaldehyde (37 wt % in H_2O) were used to synthesize the resol precursor.[38] Cobalt(III) acetylacetonate ($Co(C_5H_7O_2)_3$, 98+%, Strem Chemicals, Inc.) and vanadyl acetylacetonate ($VO(C_5H_7O_2)_2$, 98%, Strem Chemicals, Inc.) served as cobalt oxide and vanadium oxide precursors, respectively. Sodium sulfate (>99%, Aldrich) was used as received and utilized as the salt in the electrolyte for electrochemical measurements.

Sample Preparation. Resol precursor was prepared by the polymerization of phenol and formaldehyde under a basic environment as described previously.[38] Following synthesis, the resol was dissolved in tetrahydrofuran (THF) at 30 wt %. Mesostructured polymer-resins (similar to FDU-16)[38] were templated by using triblock copolymer F127 with molar compositions of phenol/formaldehyde/NaOH/F127 = 1:2:0.1:0.006.[38] For preparing nanocomposite film, $Co(acac)_3$ or $VO(acac)_2$ was added into resol and F127 in THF solution with fixed molar ratio of resol/F127 = 1:0.006. To maintain the same thickness range for all the films, all the solutions are diluted to 10 wt % of solids (i.e., F127 + resol + Metal(acac)). Silicon wafers were cleaned in piranha solution for 20 min at 90 °C and used as substrates. Films were prepared by spin-coating at 4000 rpm for 45 s on clean silicon wafer. The films were aged at room temperature for 1 h, and subsequently the resol is thermopolymerized at 120 °C for 24 h to solidify the network. These as-made films are denoted as FDU16-am (pure carbon) and CM-X-am, where M represents the metal included in the composite and X lists the weight percent of M(acac) in the as-made (am) film. The pluronic template was removed thermally by pyrolysis in nitrogen. Mesoporous polymer composite films (CM-X-350) were obtained after pyrolysis at 350 °C for 3 h using a heating rate of 1 °C/min, whereas mesoporous carbon composites (CM-X-800) were obtained after carbonization at 800 °C for 3 h, with heating rates of 1 °C/min below 600 °C, and 5 °C/min above 600 °C.

Characterization Techniques. X-ray diffraction (XRD) was performed in a $\theta/2\theta$ geometry using Cu Kα source (Panalytical X'Pert

Table 1. Porosity, Conductivity, and Chemical Compositions of the Mesoporous Carbon/Carbon−Cobalt Composite Films

sample -800 °C	M(acac) (g)	resol (g)	F127 (g)	porosity (%)	Co / V[a] (wt %)	conductivity (S/cm)	C/M[b]/H[c] (molar ratio)
FDU16	0.00	0.40	0.20	23	0.0	22	1/0/0.12
CCo-10	0.05	0.50	0.25	35	4.7	42	1/0.01/0.056
CCo-20	0.10	0.40	0.20	29	17.5	32	1/0.045/0.5
CCo-33	0.10	0.20	0.12	25	25.3	26	1/0.07/0.2
CV-10	0.05	0.50	0.25	30	2.9	41	1/0.007/0.08
CV-20	0.10	0.40	0.20	31	11.2	38	1/0.03/0.11
CV-33	0.10	0.20	0.12	24	20.0	33	1/0.06/0.22
CV-50	0.10	0.10	0.06	20	36.5	20	1/0.14/0.41

[a] Based upon only C, Co, V, and H content while neglecting oxygen. [b] M = metal (either Co or V). [c] Determined from RBS measurements of the thin films.

PRO) with angle of incidence, θ, varied from 0.25 to 1.5°. A parallel plate collimator (PPC) was used in combination with an incident beam optical module to provide an X-ray beam with very low divergence. Rutherford back scattering (RBS) was performed to obtain the elemental composition of the samples using IBeAM (Ion Beams for Analysis of Materials) facility at ASU with 1.7×10^6 tandem electrostatic accelerator sample analysis end stations. Elastic recoil detection (ERD) analysis was used to quantify hydrogen content.

Film thickness and the optical properties of the films were quantified using a UV−visible−NIR (240−1700 nm) variable angle spectroscopic ellipsometer (VASE M-2000, J.A. Woollam Co. These data provide a route to the optical properties of the films based upon the Cauchy model with an Urbach adsorption for the as-made films and films after pyrolysis at 350 °C, while an oscillator model based upon multiple Gaussian functions was used for films after pyrolysis at 800 °C. Ellipsometric porosimetry (EP) was utilized to provide the pore size distribution and the porosity of the pyrolyzed films using the same M-2000 instrument. Toluene (Aldrich) was utilized as the probe molecule. The change in refractive index of films during the pore filling/emptying provides vapor adsorption/desorption isotherms as a function of toluene partial pressure.[40−42] Assuming all pores were filled and neglecting the minor film swelling, the film porosity (P) was estimated from the refractive index of the film using the Bruggemann effective medium approximation (BEMA).[43] To quantify the pore size distribution (PSD), the radius of mesopore, r_p, was calculated as the sum of the Kelvin radius and the thickness of the absorbed layer prior to capillary condensation.[40,41] Each isotherm was fit to an arbitrary function based upon a series of Gaussian and Sigmoid functions[44] to provide a smooth curve for differentiation to estimate the population of pore sizes.[40−42]

TEM and scanning TEM (STEM) were performed on cross sections of the films using JEOL 2010F microscope operating at 200 keV. TEM cross-section samples were prepared by manually polishing, dimpling, and then ion-milling. First, the film-wafer was broken into 2 pieces that were glued together, face-to-face, to protect the film from the mechanical sample preparation. The thickness of the center of the bonded wafers was decreased to under 10 μm by polishing and dimpling processes. Ion milling was used to further decrease the thickness until a small hole was sputtered in the center of the glue line. TEM images were obtained along the glue line of the two films where the samples were properly thinned for transmission measurements. During STEM measurements, elemental analysis was performed for select samples using electron energy loss spectroscopy (EELS) to determine binding of the metal centers. Additional characterization of the binding of the Co and V was performed using X-ray photoelectron spectroscopy (XPS, Microtech, Fisons Instruments).

The electrical conductivity of the films was determined using a four-point probe system (SP4-40045TFS, Lucas Laboratories). The current was sourced (Keithley 6221 AC and DC Current Source) across pins 1 and 4, while the potential was measured across the inner pins using an Agilent U1251A Digital Multimeter (DMM) according to typical protocols. The conductivity was corrected for the film thickness using typical geometric arguments.[45] Electrochemical measurements were carried out in a three electrode cell with a Pt wire counter electrode and Hg/Hg_2SO_4 reference electrode using a CHI630 electrochemical analyzer (CH Instruments Inc.). Molybdenum was sputtered onto the silicon substrate to serve as the current collector for electrochemical measurements. Electrochemical tests were conducted in 1 M Na_2SO_4 at ambient temperature with aqueous potentials referenced against Hg/Hg_2SO_4.

RESULTS AND DISCUSSION

Morphology of Mesoporous Polymer/Carbon−Cobalt Composite Films. Mesoporous carbon−cobalt oxide composite films are synthesized using resol and $Co(acac)_3$ as precursors with Pluronic F127 as the templating agent. Table 1 shows the formulations utilized to synthesize these mesoporous composite films. As the $Co(acac)_3$ content in the as-made films is increased from 10 to 33 wt %, there is a corresponding increase in the final Co concentration in the carbonized films based on RBS results. One difficulty in fully quantifying the film composition is interference in the oxygen signal from the native oxide of the silicon wafer because of the film thickness being insufficient to fully adsorb scattering from the buried interface. For this reason, only the carbon, cobalt, and hydrogen content is reported; for the films described previously the Co content increases from 4.7 to 25.3 wt % when only considering element C, Co, and H. As the cobalt is oxidized to CoO (as determined from XPS and EELS measurements; see Supporting Information for these data), this calculation overestimates the cobalt content, but underestimates the noncarbon content of the composite. Nonetheless, the addition of $Co(acac)_3$ to the casting solution provides a simple route to incorporation of heteroatoms in mesoporous carbon films.

To determine if the templated pore structure is preserved with the addition of $Co(acac)_3$ to the precursor, XRD is initially utilized as a screening tool for the ordered structure. For the as-made films, only a single diffraction peak is observed except for CCo-33 a.m., which does not show any evidence of an ordered structure (Figure 1A). The lack of higher order reflections may result from the limited contrast in electron density between phenolic resol and surfactant in the as-made film; the addition of the $Co(acac)_3$ is expected to only slightly increase the contrast if segregated to the hydrophilic domain. A single diffraction peak for the as-made films is consistent with prior results for thicker

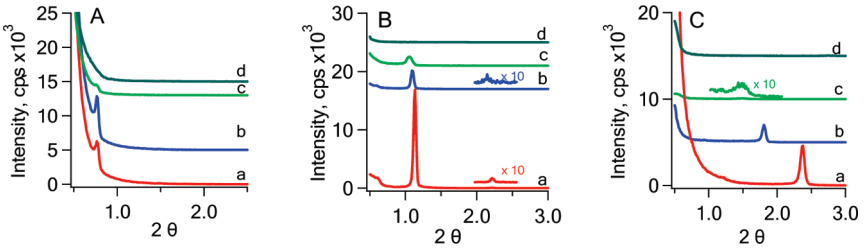

Figure 1. XRD profiles of mesoporous nanocomposite films: (a) FDU16, (b) Co-10, (c) Co-20, and (d) Co-33 for (A) as-made films, (B) films pyrolyzed at 350 °C, and (C) films pyrolyzed at 800 °C.

Table 2. *d*-Spacing from Primary Diffraction Peak and Calculated Contraction of Carbon–Cobalt/Vanadium Composite Films

sample	*d*-spacing from as made (nm)	*d*-spacing after pyrolysis at 800 °C (nm)	contraction (%)
FDU16-350	11.54	7.78	33
CCo-10-350	11.54	8.06	30
CCo-20-350	11.69	8.37	28
FDU16-800	11.54	3.72	68
CCo-10-800	11.54	4.89	58
CCo-20-800	11.69	6.15	47
CV-10-800	10.97	5.40	51
CV-20-800	10.09	4.95	51
CV-33-800	11.10	4.89	56

films of resol-surfactant.[46] After removal of the template at 350 °C, two diffraction peaks are now observed for both FDU16-350 and CCo-10-350 (Figure 1B); additionally, the intensities of the primary peaks are substantially greater than the corresponding as-made films as expected from the increase in contrast. For all CCo-33 films, no diffraction peaks have been detected, which indicate no long-range ordered mesostructure in these materials.

Changes in the mesostructure upon pyrolysis can be elucidated from the position of the primary diffraction peak; the primary peaks shift to larger 2θ after removal of the template at 350 °C. This shift is indicative of a decrease in *d*-spacing from contraction during the pyrolysis process. The *d*-spacing is calculated using Bragg's Law, $\lambda = 2d \sin\theta$, where λ is the wavelength (1.54 Å for Cu Kα), *d* is *d*-spacing in angstroms (Table 2), and θ is the diffraction angle. From the *d*-spacings of the as-made and mesoporous polymer composite films, the contraction, *C*, is calculated as $C = (d_{am} - d_{350})/d_{am}$, while d_{am} is the *d*-spacing for as-made films and d_{350} is the *d*-spacing for films pyrolyzed at 350 °C. Table 2 illustrates the difference in contraction for the mesoporous polymer composite films from the *d*-spacing. These contraction results show that addition of Co tends to reduce the contraction of mesoporous ordered structure films during pyrolysis at 350 °C.

Carbonization of the film at 800 °C results in further contraction as evidenced by the primary diffraction peak shifting to even larger 2θ (Figure 1C). However, it can be easily observed that this shift is decreased as Co concentration increases, indicating a larger *d*-spacing and lower contraction. Thus, the contraction is significantly decreased as Co concentration increases, similar effects result from adding SiO_2 into the film[46]as quantified in Table 2. This compositional dependence of the *d*-spacing suggests that Co is distributed within the carbon framework.

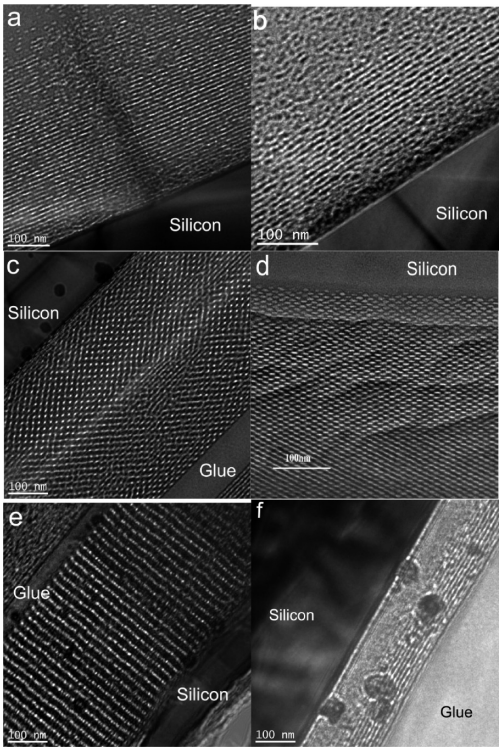

Figure 2. Cross-section TEM micrographs of mesoporous nanocomposite films after pyrolysis: (a) FDU16-350, (b) Co-10-350, (c) Co-20-350, (d) FDU16-800, (e) Co-10-800, and (f) Co-20-800.

To examine the mesostructure in more detail, TEM is utilized as shown in Figure 2. In agreement with the previously discussed XRD results, micrographs of FDU16-350 (Figure 2a), CCo-10-350 (Figure 2b), and CCo-20-350 (Figure 2c) films exhibit a highly ordered mesostructure after pyrolysis at 350 °C. In all cases, the mesopores appear to be nearly spherical in nature and distributed on a near cubic lattice. Further pyrolysis of these films to carbonize the phenolic resin at 800 °C indicate the highly ordered mesoporous structure is stable as shown in the micrographs of FDU16-800 (Figure 2d), Co-10-800 (Figure 2e), and CCo-20-800 (Figure 2f). One difference is for the CCo-20-800 film where the bottom layer of the film is only slightly porous, while the near surface has large domains of regular pores (Figure 2f). Also examining the mesopores in detail, an obvious distortion of the pores is observed to an asymmetric elliptical shape with the pore dimension significantly smaller through the thickness of the film. Additionally, the pore size is significantly decreased in comparison to films pyrolyzed at 350 °C. The short

dx.doi.org/10.1021/cm2002429 |*Chem. Mater.* 2011, 23, 2869–2878

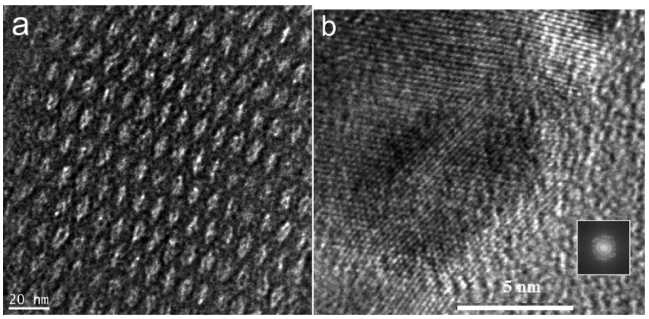

Figure 3. HR-TEM of (a) Co-10-800 and (b) Co-20-800 films. For the Co-20-800 film, the micrograph shows the lattice fringes from CoO nanoparticle.

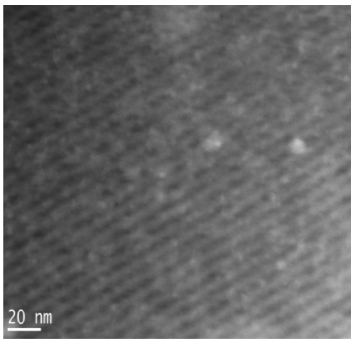

Figure 4. STEM micrograph of Co-10-800 film. The bright spots are Co, darker area is carbon and black areas are pores.

axis of the mesopores increases from 1.8 nm for FDU16-800 to 3.6 nm for CCo-10-800, which is consistent with the *d*-spacing changes determined from XRD. During pyrolysis process at 800 °C, all the components in the precursor are "soft" organic compounds for FDU16-800 and a large contraction (68%) is observed. However for carbon cobalt composites, the presence of rigid CoO that forms from the decomposition of $Co(acac)_3$ appears to effectively reduce the framework shrinkage (58% for CCo-10-800 and 47% for CCo-20-800), and hence the mesopores derived from degradation of F127 maintain a larger pore radius than FDU16-800.[19] This contraction can also be clearly observed from the cross-section TEM images. For example, the CCo-20-350 film that is 478 nm thick (Figure 2c) decreases to 183 nm upon carbonization (Figure 2f). This fractional thickness decrease (60%) is much larger than expected from the decrease in *d*-spacing determined from XRD. The lack of mesopores in the lower fraction of the film could explain this discrepancy as collapse of the mesostructure would lead to a decrease in the film thickness, while not impacting the location of the primary diffraction peak that results solely from the ordered mesoporous regions. In addition to the mesopores, nanoparticles are also clearly visible in the micrographs for CCo-10-800 (Figure 2e) and CCo-20-800 (Figure 2f). For CCo-10-800, the nanoparticles are distributed throughout the film with the nanoparticle size less than 20 nm. Conversely for CCo-20-800, very large particles are observed that are greater than 80 nm in some cases. This suggests that the cobalt particles ripen during the carbonization process and could provide an explanation for the lack of ordered structure at high $Co(acac)_3$ loadings.

To further investigate the structure of these films, HR-TEM is employed. When examining the local structure of the ordered mesoporous region, HR-TEM illustrates small nanoparticles (1−2 nm) within the carbon framework (Figure 3a) of Co-10-800 film. These nanoparticles within the carbon framework are likely responsible for the decreased contraction in comparison to FDU16-800 film. Figure 3b shows a HR-TEM micrograph of a larger particle in Co-20-800 film; the micrograph shows randomly oriented lattice fringes in the darker area, but the bright area surrounding the dark nanoparticle also illustrates randomly oriented lattice fringes as well. Additionally, the live Fast Fourier Transform pattern also displays a ring diffraction pattern (inset in Figure 3b), which illustrate the polycrystalline structure of the particle. We hypothesize that the particles are carbon/cobalt oxide core−shell crystalline nanocomposites. This structure is consistent with the direct pyrolysis of $Co(acac)_3$ at 800 °C that yields a carbon/Co oxide core−shell structure nanocomposites.[47]

To further investigate the structure of the Co-10-800 film as the nanoparticles are difficult to visualize in the HR-TEM micrographs, z-contrast STEM has been utilized to investigate the nanoparticles distribution as illustrated in Figure 4. The contrast in the system is based on the atomic number with lighter areas associated with larger atomic numbers; in this case, the bright white spots are attributed to Co-based nanoparticles. Although there are a few aggregated particles (approximately 10 nm in diameter) in the film, most nanoparticles are dispersed throughout the wall framework as sub-1 nm particles based upon the micrograph. The is a significant difference in the distribution and size of the cobalt oxide nanoparticles between the Co-10-800 and Co-20-800; although the total cobalt content is larger for Co-20-800, there appear to be significantly more small nanoparticles for Co-10-800 based upon TEM and STEM micrographs.

Pore size distribution and porosity play a vital role in mechanical, thermal, and chemical properties of the porous films and their feasibility to be used in microelectronic technology.[37,38] The ellipsometric porosimetry (EP) method is a powerful technique to characterize the mesopores in thin films, which utilizes adsorption/desorption isotherms of the changes of refractive index caused by the various partial pressures of an organic solvent around a film.[37] Figure 5a shows the adsorption/desorption isotherms of Co-10-350 film, which is a typical type-IV isotherm with an H_1-type hysteresis loop. These isotherms are representative of those obtained for the mesoporous carbon composite films examined; adsorption/desorption isotherms for the other composite films are presented as Supporting Information. The Kelvin equation is then utilized with the EP data to estimate the pore size distribution (PSD) of the films. The pore size distribution of Co-10-350 calculated from the desorption isotherm is shown in Figure 5b.

Similarly, Figure 6a shows the pore size distribution for all the polymer-Co films after the removal of template at 350 °C; a narrow distribution is found for all films as would be expected for a templated synthesis. The average pore radius increases from approximately 2 to 3 nm when $Co(acac)_3$ concentration increases in the precursor film from 0 to 20 wt %. This increase in the average pore size is consistent with the decreased contraction determined from XRD, which would be expected to lead to larger pore size and higher porosity. The corresponding carbonized films also show a marked increase in the average pore size at larger Co concentration. Because of further contraction from pyrolysis at 800 °C, the average pore size of all the carbon-Co

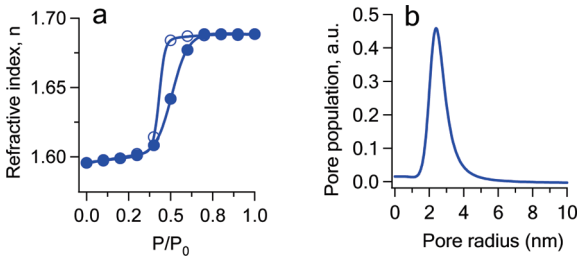

Figure 5. (a) Toluene adsorption and desorption isotherms (a, c, e, and g) in mesoporous nanocomposite films as determined through the changes in the refractive index (λ = 632.4 nm) of the Co-10-350 film as a function of the adsorbate (toluene) relative pressure. Closed symbol lines are for the adsorption process and the open symbol lines are desorption isotherms. (b) Pore size distribution of Co-10-350 film calculated by the Kelvin equation using desorption isotherms.

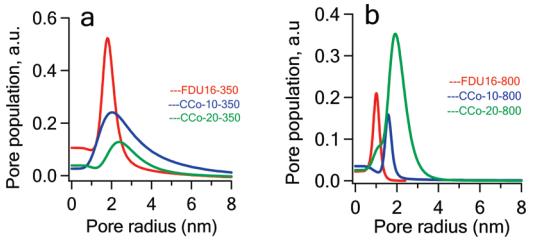

Figure 6. Pore size distributions of (a) polymer-Co films and (b) carbon-Co films.

films (Figure 6d) is approximately 1 nm smaller than corresponding mesoporous polymer composite films (350 °C).

Morphology of Mesoporous Polymer/Carbon−Vanadium Composite Films. To investigate the applicability of this triconstituent assembly to other organometallics, similar materials are synthesized with $VO(acac)_2$ substituting for $Co(acac)_3$. The composition of the vanadium containing mesoporous composite films is shown in Table 1. Similar to carbon−cobalt films, the ordered structure of the films is examined using XRD. All as-made films of the carbon−vanadium-based nanocomposites exhibit a single diffraction peak that is similar to the vanadium free analogue (FDU16 a.m. film) when the $VO(acac)_2$ concentration is lower than 50% as shown in Figure 7a. Removal of the surfactant template results in a shift in the primary diffraction peaks to larger 2θ. As the pyrolysis temperature is increased, the films contract further as evidenced by the shift in the primary diffraction peak (Figure 7b). The compositional dependence of the contraction and d-spacings are tabulated for both vanadium and cobalt-based composite films in Table 2 for polymer and carbon composites, respectively. Both CV-10-350 and CV-20-350 films contract (30% for CV-10-350 and 28% for CV-20-350) less than FDU16-350; this is consistent with increasing mechanical rigidity of the porous framework from the incorporation of vanadium (or cobalt as discussed in the prior section). However, CV-33-350 film has a slightly larger contraction than FDU16-350; this could be a result of long-range order loss with high concentration of $VO(acac)_2$ in the film as CV-50-am does not appear to be ordered. After pyrolysis at 800 °C (Table 2), the increase in contraction for the composite films from the 350 °C is reduced in comparison to pure carbon. Both CV-10-800 and CV-33-800 films exhibit a single diffraction peak at relatively low 2θ that corresponds to a d-spacing of 5.4 nm (2θ = 1.635°) and 4.9 nm (2θ = 1.805°), respectively. This suggests that addition of V into the carbon film significantly reduces the framework contract from stresses developed during carbonization process.

To confirm the ordered mesoporous structure suggested from the XRD profiles, the films are examined using TEM for a real-space image. The polymer-vanadium films show a highly ordered mesoporous structure similar to polymer-cobalt films after pyrolysis at 350 °C (Figure 8a and 8b). However, it is interesting that after pyrolysis at 800 °C for 3 h, the ordered mesostructure appears to be more wormhole-like, than a near cubic arrangement of isolated mesopores (Figures 8c and 8d). However, it would be highly unusual for a high temperature transition in the mesostructure to occur between 350 and 800 °C that could provide an explanation of the differences in the apparent mesostructures in the TEM micrographs shown in Figure 8. Unlike the carbon−cobalt oxide mesoporous composite films, the vanadium-based analogues do not show any large nanoparticles (or aggregates). To investigate the morphology of the films in most detail, z-contrast STEM has been utilized. Figure 9 illustrates the mesostructure of CV-10-800 as determined from STEM. The cross section shows most nanoparticles are small (<5 nm, bright spots) and distributed within the carbon framework. Interestingly, the pores in the sample (dark spots) appear to actually be organized on a lattice as expected for a near cubic structure. The ordered structure of carbon−vanadium carbonized may appear to be wormhole-like in the TEM image because of the scattering and reflection of electrons from vanadium oxide nanoparticles that could be randomly distributed in the framework.

For PSD in carbon−vanadium films, CV-10-350 film exhibits the largest average pore radius (2.7 nm, Figure 10a) among all the polymer-V composite films, which is supported by XRD results that CV-10-350 film has the smallest contraction. Corresponding to XRD results, CV-20-350 and CV-33-350 films maintain about the same pore size as pure FDU16-350 film. However, after pyrolysis at 800 °C (Figure 10b), from PSD results, all the carbon-V films show a larger pore radius (1.4 nm for CV-10-800, 1.6 nm for CV-10-800, and 1.5 nm for CV-20-800) than FDU16-800 (1 nm), which is also consistent with contraction results that carbon-V films contract much less than pure carbon films.

Electrochemical Performance of Mesoporous Carbon Composite Films. Ordered mesoporous materials generally exhibit high specific surface areas, which are attractive for electrochemical applications. One issue in many cases is the poor electrical conductivity of the active material that necessitates addition of conductive filler such as carbon black.[19] To first assess any electrical conductivity limitations of the mesoporous composite films, a four-point probe test has been used, and relatively high conductivity is found for all the films. As shown in Figure 11, the conductivity of the carbon film can be increased by addition of 10 wt % of either $Co(acac)_3$ or $VO(acac)_2$ into the precursor solution, The conductivity increases from approximately 22 S/cm for the pure mesoporous carbon film (in agreement with previous studies for FDU-16 carbonized at 800 °C)[48,46] to approximately 40 S/cm. Addition of more organometallic decreases the electrical conductivity, but both Co-33-800 film (26 S/cm) and V-50-800 (20 S/cm) are comparable in conductivity to the neat carbon, FDU16-800. Interestingly, the conductivity of the cobalt-based composites decreases more at equivalent organometallic loading in comparison to the vanadium-based composite films; the size of nanoparticle inclusions in the mesoporous films may be important to electrical conduction as the cobalt nanoparticles are larger. Previous studies of nickel oxide

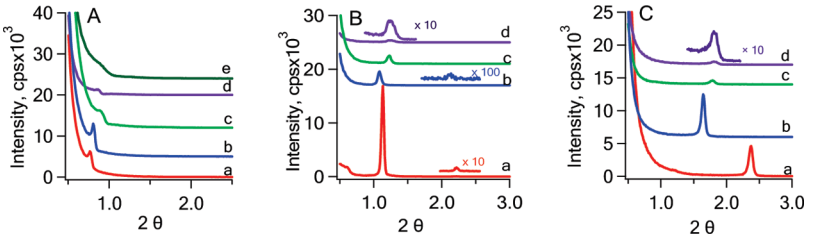

Figure 7. XRD profiles of mesoporous structure nanocomposite films: (a) FDU16, (b) CV-10, (c) CV-20, (d) CV-33, and (e) CV-50 for (A) polymer-V as-made films, (B) films pyrolyzed at 350 °C, and (C) films pyrolyzed at 800 °C.

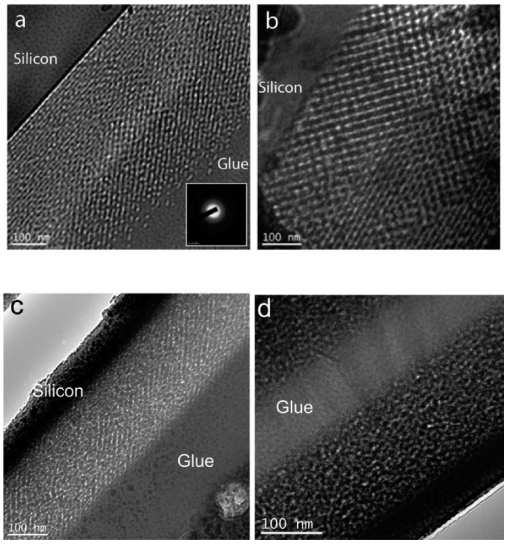

Figure 8. Cross-section TEM micrographs of mesoporous nanocomposite films: (a) CV-10-350, (b) CV-20-350, (c) CV-10-800, and (d) CV-33-800.

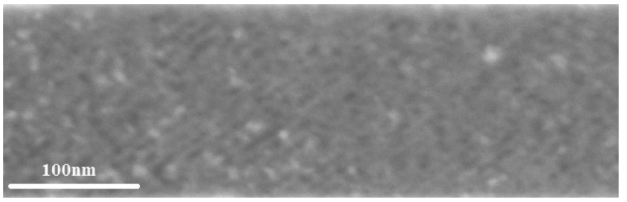

Figure 9. STEM micrograph of CV-10-800 film. The bright spots are vanadium, the darker area is carbon, and the black area are pores.

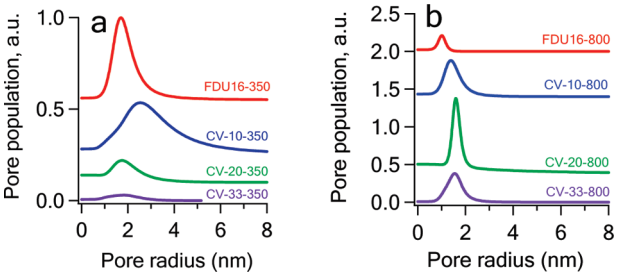

Figure 10. Pore size distributions of (a) polymer-V films and (b) carbon-V films.

nanoparticles showed a significant increase in electrical conductivity for 5 nm nanoparticles in comparison to larger nanoparticles;[49] this enhancement was attributed to an increase in the defect density of the oxide. A similar effect is likely responsible for the enhanced conductivity of the cobalt oxide and vanadium oxide−carbon mesoporous composite films. Additionally, there may also be some enhancement in the conductivity from the formation of a graphitic shell around the nanoparticles as suggested by the HR-TEM micrograph shown in Figure 3b. The graphitic shell is evidenced by its lighter fringes surrounding the much darker crystalline CoO particle. Nonetheless, all the mesoporous composite films exhibit relatively high electrical conductivity that should facilitate electrochemical processes.

To examine the (pseudo)capacitive properties of the films, cyclic voltammetry measurements are utilized for all the Co−C and V−C carbonized films at 100 mV s^{-1} using 1 M aqueous Na_2SO_4 for the electrolyte. Figure 12 illustrates the cyclic voltammograms for the composite films; the profiles are relatively flat and rectangular, which is typical for electrochemical double-layer capacitors.[19,21] Even at relatively fast rates (100 mV/s), the capacitance of the films is appreciable. To quantify the capacitance of the films for direct comparison, the mass of films is estimated from the film area exposed to the electrolyte, film thickness and the film porosity using the density of graphite (2.27 g/cm^3). This calculation overestimates the mass of the film as the density of the amorphous carbon is generally between 1.8 and 2.1 g/cm^3; thus, the capacitance for the films reported here is a conservative estimate. By assuming that the rate of electron transfer between the materials and the solution is negligible, we can calculate the capacitance of the films as $C = dQ/dV$, where C is capacitance, Q is the charge, and V is the potential.[43] For the pure mesoporous carbon film (FDU16-800), a capacitance of 22 F/g is observed for the first cycle. This capacitance agrees well with the capacitance for a mesoporous carbon powder with similar porosity and pore size (28 F/g at 2 mV/s).[21] The addition of the organometallic precursors can significantly increase the capacitance of the films; this is expected through the added pseudocapacitance of both cobalt oxide[50] and vanadium oxide.[51] For the cobalt-based films, the first cycle capacitance increases significantly with the added nanoparticles to 116 F/g for CCo-10-800 to 125 F/g for CCo-20-800. This capacitance is actually larger than a pure Co_3O_4 film (74 F/g).[50] This enhanced capacitance is likely a result of both the accessibility of the cobalt oxide in the mesoporous carbon framework and the electrical conductivity imparted by the continuous carbon framework. Interestingly, the capacitance of the film actually decreases with further increases in the cobalt content, which also corresponds to a loss in the ordered mesostructure (see Figure 1).

dx.doi.org/10.1021/cm2002429 |*Chem. Mater.* 2011, 23, 2869–2878

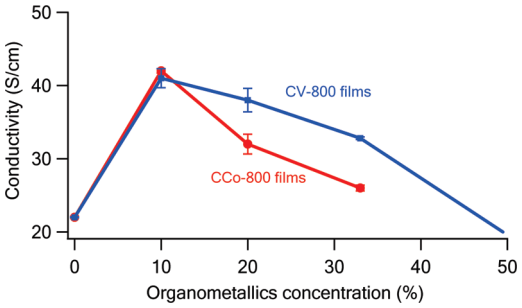

Figure 11. Electrical conductivity of films pyrolyzed at 800 °C is shown as a function of $Co(acac)_3/VO(acac)_2$ concentration in the precursor solution. Error bars represent standard deviation of 4 independent measurements.

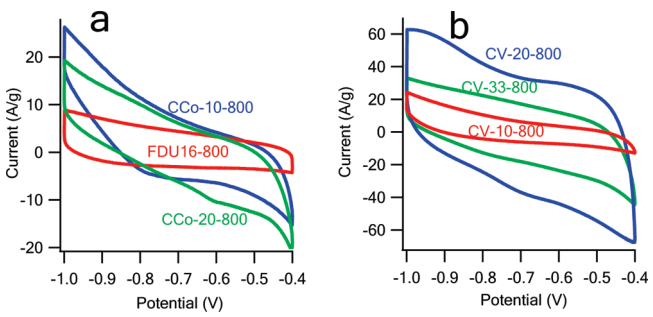

Figure 12. Cyclic voltammetry at 100 mV/s scan rate for (a) Co-based and (b) V-based composite mesoporous films in 1 M Na_2SO_4.

Major differences in these films are the ordered mesoporous framework (disordered at high $Co(acac)_3$ loadings and the size of the cobalt nanoparticles (increases at higher loadings), which might adversely impact the electrochemical performance. To further decouple the impact of nanoparticle size and film pore structure, the vanadium-based composite films can be examined as the nanoparticle size is relatively independent of $VO(acac)_2$ loading in the precursor film. Interestingly, the initial capacitance of the films increases steadily as the vanadium content is increased CV-10-800 (55 F/g), CV-20-800 (64 F/g), CV-33-800 (150 F/g), and CV-50-800 (215 F/g). The combined results from the CV and CCo films suggest that the nanoparticle size may be a critical parameter for the capacitance of these mesoporous composites as the capacitance increases with increasing organometallic loading for the CV films that contain small nanoparticles, but there is an apparent optimum for the CCo films, which corresponds with a significant increase in the size of the CoO nanoparticles within the film. This increased capacitance for the smaller nanoparticles is consistent with results for hydrated RuO_2 powders;[52] the size dependence is attributed to surface utilization and mass transport limitations. We hypothesize similar origins to the observed capacitance behavior of the mesoporous carbon composite films as the mesopores should provide minimal transport limitations at the scan rates examined.

In addition to the initial capacitance of the films, the cyclic performance is critical to any electrochemical energy storage application. Figure 13 illustrates the capacitance for the different mesoporous carbon composite films for 500 charge/discharge cycles. For FDU16-800 and Co-10-800, the specific capacitances are stable around 22 F/g and 115 F/g, respectively, for these

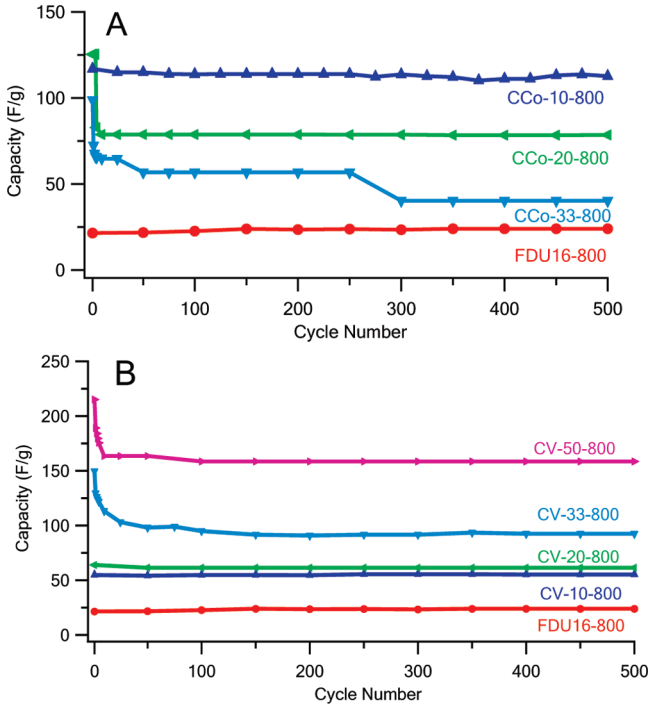

Figure 13. Cycle performance of (A) C−Co films and (B) C−V films.

500 cycles. Conversely, the specific capacitance of Co-20-800 decreases rapidly to 83 F/g (maintains 66% of initial capacitance) after 5 cycles, but then only decreases slightly further to 78 F/g (maintains 62%) after 500 cycles. Further increasing the cobalt content results in a similar severe and rapid decrease in specific capacitance. For example, the capacitance of Co-33-800 decreases from 99 F/g to 72 F/g after only 2 cycles; interestingly, this capacitance is not stable with a further decrease in capacitance down to 40 F/g through 500 cycles. The capacitance loss is typically attributed to irreversible reactions of electrolyte with adsorbed impurities on the surface of the electrode. However, this instability is most pronounced for the higher Co ($Co(acac)_3$ > 10% in precursor) loadings and suggests that the structure of the metal oxide is primarily responsible for the loss in capacitance. For carbon−vanadium carbonized films (Figure 13b), the lower capacitance films (FDU16-800, CV-10-800, and CV-20-800) are nearly invariant with electrochemical cycling. However, the capacitance of CV-50-800 drops from 215 to 160 F/g (maintains 74%) and CV-33-800 drops from 150 to 103 F/g (maintains 69%) after only 10 cycles. However, the capacitance of these films is only slightly decreased upon further cycling (up to 500 cycles).

An unusual observation from these electrochemical measurements on the mesoporous carbon composite films is that the specific capacitance does not necessarily always increase with the pseudocapacitive metal oxide content. For the vanadium-based composites, there is a direct correlation between specific capacitance and vanadium content. Conversely for carbon−cobalt films, the average specific capacitance actually decreases with cobalt content. One major difference in these sample sets is the dispersion and size of the metal oxide nanoparticles. There is limited aggregation of nanoparticle in the carbon−vanadium films with the V distributed relatively uniformly in the film. However, for the carbon−cobalt films, higher Co concentration leads to larger (or aggregated) particles, and a nonuniform texture is observed in these films. Thus similar to traditional heterogeneous

catalysts, good dispersion of small nanoparticles might be ideal for electrochemical applications based upon these limited results. Additional work that systematically varies the nanoparticle size in a conductive framework would be useful to understand the relationship between nanoparticle size and electrochemical performance. Nonetheless, these ordered mesoporous carbon composite films appear to possess attractive electrical and electrochemical properties for energy storage applications.

CONCLUSIONS

Ordered mesoporous carbon composite films are synthesized using triconstituent self-assembly of resol (carbon precursor), an acac-based organometallic (metal oxide precursor) and Pluronic F127 (structure directing agent). The ordered morphology is confirmed using X-ray diffraction and TEM for both vanadium and cobalt containing composite films. There exists an upper limit for the organometallic content to maintain an ordered mesostructure that is precursor dependent. The size of the nanoparticle inclusions in the carbon framework is also dependent upon the organometallic precursor. For $Co(acac)_3$, small isolated nanoparticles are observed at low loading (10 wt %), but much larger aggregates/nanoparticles are observed at higher loadings(20 wt %). Conversely, small dispersed nanoparticles are observed for all compositions examined when using $VO(acac)_2$ as the organometallic precursor. These morphological differences appear to significantly impact the electrical and electrochemical properties of these films. The electrical conductivity increases initially with the introduction of either V or Co to 10 wt % of the organometallic in the precursor film, but then decreases with further loading down to approximately the same conductivity as the initial pure carbon film at the highest $VO(acac)_2$ and $Co(acac)_3$ loadings examined. However, the conductivity of the films remains greater than 20 S/cm for all films and thus, electrical resistance should not be a limiting factor in electrochemical measurements. The capacitance of the mesoporous films is more strongly dependent upon the choice of organometallic precursor. As the concentration of $VO(acac)_2$ is increased in the precursor films, the composite carbon film capacitance is increased. There is a decrease in the electrochemical stability of the capacitance as $VO(acac)_2$ content is increased beyond 20 wt %; but even after 500 cycles, the capacitance is still greatest for the highest V content film. Conversely, the capacitance of the Co−C composite films is greatest for the 10 wt % $Co(acac)_3$ film. This result suggests that the small dispersed nanoparticles are most effective for increasing the capacitance of carbons.

ASSOCIATED CONTENT

Supporting Information. Additional adsorption/desorption isotherms obtained from ellipsometric porosimetry, XPS, and EELS data. This material is available free of charge via the Internet at http://pubs.acs.org.

AUTHOR INFORMATION

Corresponding Author

*E-mail: bryan.vogt@asu.edu.

Present Addresses

[§]Praxair, Inc., 175 East Park Drive, Tonawanda, NY 14150.

ACKNOWLEDGMENT

This work is financially supported by the National Science Foundation under Grant CBET-0746664. Acknowledgment is made to the Donors of the American Chemical Society Petroleum Research Fund for partial support of this research through Grant 49218-DNI7. We acknowledged the support of the Center for Solid State Electronics Research and Center for Solid State Science for research facilities used in this work.

REFERENCES

(1) Liang, C. D.; Li, Z. J.; Dai, S. *Angew. Chem., Int. Ed.* **2008**, *47*, 3696.
(2) Schuth, F. *Chem. Mater.* **2001**, *13*, 3184.
(3) Gao, P.; Wang, A.; Wang, X.; Zhang, T. *Chem. Mater.* **2008**, *20*, 1881.
(4) Liu, C. Y.; Chen, C. F.; Leu, J. P.; Lu, C. C.; Liao, K. H. *Sens. Actuators, B* **2009**, *143*, 12.
(5) Wang, G. Q.; Xing, W.; Zhuo, S. P. *J. Power Sources* **2009**, *194*, 568.
(6) Baniamerian, M. J.; Moradi, S. E.; Noori, A.; Salahi, H. *Appl. Surf. Sci.* **2009**, *256*, 1347.
(7) Lee, J.; Yoon, S.; Hyeon, T.; Oh, S. M.; Kim, K. B. *Chem. Commun.* **1999**, 2177.
(8) Ryoo, R.; Joo, S. H.; Jun, S. *J. Phys. Chem. B* **1999**, *103*, 7743.
(9) Meng, Y.; Gu, D.; Zhang, F. Q.; Shi, Y. F.; Yang, H. F.; Li, Z.; Yu, C. Z.; Tu, B.; Zhao, D. Y. *Angew. Chem., Int. Ed.* **2005**, *44*, 7053.
(10) Kosonen, H.; Valkama, S.; Nykanen, A.; Toivanen, M.; ten Brinke, G.; Ruokolainen, J.; Ikkala, O. *Adv. Mater.* **2006**, *18*, 201.
(11) Liang, C. D.; Hong, K. L.; Guiochon, G. A.; Mays, J. W.; Dai, S. *Angew. Chem., Int. Ed.* **2004**, *43*, 5785.
(12) Tanaka, S.; Katayama, Y.; Tate, M. P.; Hillhouse, H. W.; Miyake, Y. *J. Mater. Chem.* **2007**, *17*, 3639.
(13) Liang, C. D.; Dudney, N. J.; Howe, J. Y. *Chem. Mater.* **2009**, *21*, 4724.
(14) Gorka, J.; Jaroniec, M. *J. Phys. Chem. C* **2008**, *112*, 11657.
(15) Kwon, T.; Nishihara, H.; Itoi, H.; Yang, Q. H.; Kyotani, T. *Langmuir* **2009**, *25*, 11961.
(16) Calvillo, L.; Moliner, R.; Lazaro, M. J. *Mater. Chem. Phys.* **2009**, *118*, 249.
(17) Hu, Q. Y.; Kou, R.; Pang, J. B.; Ward, T. L.; Cai, M.; Yang, Z. Z.; Lu, Y. F.; Tang, J. *Chem. Commun.* **2007**, 601.
(18) Liu, R. L.; Shi, Y. F.; Wan, Y.; Meng, Y.; Zhang, F. Q.; Gu, D.; Chen, Z. X.; Tu, B.; Zhao, D. Y. *J. Am. Chem. Soc.* **2006**, *128*, 11652.
(19) Li, H. Q.; Liu, R. L.; Zhao, D. Y.; Xia, Y. Y. *Carbon* **2007**, *45*, 2628.
(20) Zhao, X.; Wang, A.; Yan, J.; Sun, G.; Sun, L.; Zhang, T. *Chem. Mater.* **2010**, *22*, 5463.
(21) Patel, M. N.; Wang, X. Q.; Wilson, B.; Ferrer, D. A.; Dai, S.; Stevenson, K. J.; Johnston, K. P. *J. Mater. Chem.* **2010**, *20*, 390.
(22) Lou, X. W.; Deng, D.; Lee, J. Y.; Archer, L. A. *Chem. Mater.* **2008**, *20*, 6562.
(23) Bruce, P. G.; Scrosati, B.; Tarascon, J. M. *Angew. Chem., Int. Ed.* **2008**, *47*, 2930.
(24) Chou, S. L.; Wang, J. Z.; Sun, J. Z.; Wexler, D.; Forsyth, M.; Liu, H. K.; MacFarlane, D. R.; Dou, S. X. *Chem. Mater.* **2008**, *20*, 7044.
(25) Das, S. K.; Darmakolla, S.; Bhattacharyya, A. J. *J. Mater. Chem.* **2010**, *20*, 1600.
(26) Jiao, F.; Bruce, P. G. *Adv. Mater.* **2007**, *19*, 657.
(27) Zhi, L. J.; Hu, Y. S.; El Hamaoui, B.; Wang, X.; Lieberwirth, I.; Kolb, U.; Maier, J.; Mullen, K. *Adv. Mater.* **2008**, *20*, 1727.
(28) Lou, X. W.; Li, C. M.; Archer, L. A. *Adv. Mater.* **2009**, *21*, 2536.
(29) Esmanski, A.; Ozin, G. A. *Adv. Funct. Mater.* **2009**, *19*, 1999.
(30) Li, Q. A.; Xu, J.; Wu, Z. X.; Feng, D.; Yang, J. P.; Wei, J.; Wu, Q. L.; Tu, B.; Cao, Y.; Zhao, D. Y. *Phys. Chem. Chem. Phys.* **2010**, *12*, 10996.
(31) Ishii, Y.; Kanamori, Y.; Kawashita, T.; Mukhopadhyay, I.; Kawasaki, S. *J. Phys. Chem. Solids* **2010**, *71*, 511.

(32) Wang, D. H.; Kou, R.; Choi, D.; Yang, Z. G.; Nie, Z. M.; Li, J.; Saraf, L. V.; Hu, D. H.; Zhang, J. G.; Graff, G. L.; Liu, J.; Pope, M. A.; Aksay, I. A. *ACS Nano* **2010**, *4*, 1587.
(33) Urade, V. N.; Hillhouse, H. W. *J. Phys. Chem. B* **2005**, *109*, 10538.
(34) Baumann, T. F.; Fox, G. A.; Satcher, J. H.; Yoshizawa, N.; Fu, R. W.; Dresselhaus, M. S. *Langmuir* **2002**, *18*, 7073.
(35) She, L.; Li, J.; Wan, Y.; Yao, X. D.; Tua, B.; Zhao, D. Y. *J. Mater. Chem.* **2011**, *21*, 795.
(36) Zhan, Z. Q.; Zeng, H. C. *J. Non-Cryst. Solids* **1999**, *243*, 26.
(37) Breitscheidel, B.; Zieder, J.; Schubert, U. *Chem. Mater.* **1991**, *3*, 559.
(38) Meng, Y.; Gu, D.; Zhang, F. Q.; Shi, Y. F.; Cheng, L.; Feng, D.; Wu, Z. X.; Chen, Z. X.; Wan, Y.; Stein, A.; Zhao, D. Y. *Chem. Mater.* **2006**, *18*, 4447.
(39) Zhang, F. Q.; Meng, Y.; Gu, D.; Yan, Y.; Yu, C. Z.; Tu, B.; Zhao, D. Y. *J. Am. Chem. Soc.* **2005**, *127*, 13508.
(40) Baklanov, M. R.; Mogilnikov, K. P.; Polovinkin, V. G.; Dultsev, F. N. *J. Vac. Sci. Technol., B* **2000**, *18*, 1385.
(41) Sing, K. S. W.; Everett, D. H.; Haul, R. A. W.; Moscou, L.; Pierotti, R. A.; Rouquerol, J.; Siemieniewska, T. *Pure Appl. Chem.* **1985**, *57*, 603.
(42) Boissiere, C.; Grosso, D.; Lepoutre, S.; Nicole, L.; Bruneau, A. B.; Sanchez, C. *Langmuir* **2005**, *21*, 12362.
(43) Song, L.; Feng, D.; Fredin, N. J.; Yager, K. G.; Jones, R. L.; Wu, Q.; Zhao, D.; Vogt, B. D. *ACS Nano* **2010**, *1*, 189.
(44) Lee, H. J.; Soles, C. L.; Liu, D. W.; Bauer, B. J.; Lin, E. K.; Wu, W. L.; Grill, A. *J. Appl. Phys.* **2004**, *95*, 2355.
(45) Smith, F. M. *Bell Syst. Tech. J.* **1958**, 711.
(46) Song, L.; Feng, D.; Campbell, C. G.; Gu, D.; Forster, A. M.; Yager, K. G.; Fredin, N.; Lee, H. J.; Jones, R. L.; Zhao, D.; Vogt, B. D. *J. Mater. Chem.* **2010**, *20*, 1691.
(47) Fabregt-Santiago, F.; Mora-Sero, I.; Garcia-Belmote, G.; Bisquert, J. *J. Phys. Chem. B* **2003**, *107*, 758.
(48) Li, X. X.; Larson, A. B.; Jiang, L.; Song, L. Y.; Prichard, T.; Chawla, N.; Vogt, B. D. *Microporous Mesoporous Mater.* **2011**, *138*, 86.
(49) Biju, V.; Khadar, M. A. *J. Mater. Chem.* **2001**, *36*, 5779.
(50) Shinde, V. R.; Mahadik, S. B.; Gujar, T. P.; Lokhande, C. D. *Appl. Surf. Sci.* **2006**, *252*, 7487.
(51) Jayalakshmi, M.; Mohan Rao, M.; Venugopal, N.; Kim, K. B. *J. Power Sources* **2007**, *166*, 578.
(52) Sugimoto, W.; Iwata, H.; Yokoshima, K.; Murakami, Y.; Takasu, Y. *J. Phys. Chem. B* **2005**, *109*, 7330–7338.